Applied Surface Science 705 (2025) 163492

Contents lists available at ScienceDirect

Applied Surface Science

journal homepage: www.elsevier.com/locate/apsusc

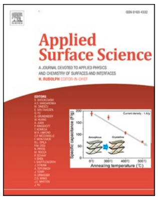

Full Length Article

Broadband synaptic photoresponse induced by the charged planar Te interlayer in epitaxial Te/GaN hybrid-heterojunction

Wenmin Li [a], Yongqi Hu [a], Xutao Zhang [a], Hao Hu [b], Yi Pan [a,*]

[a] Center for Spintronics and Quantum Systems, State Key Laboratory for Mechanical Behavior of Materials, Xi'an Jiaotong University, Xi'an 710049, China
[b] Luology (Shandong) Digital Technology Co., LTD., Weifang 261021, China

ARTICLE INFO

Keywords:
Te/GaN heterojunction
Interfacial interlayer
Broadband photoresponse
Self-powered detection
First-principles calculations

ABSTRACT

Broadband photodetection is crucial for a variety of advanced sensing applications like environmental monitoring, optical communication, and optoelectronic synapses. The emerging van der Waals (vdW) optoelectronic materials become important complementary to the conventional semiconductors, which are mostly optimized for specific spectral ranges. In this work, we report a new strategy to realize broadband synaptic photoresponse by growing the vdW material Te on III-V semiconductor GaN as an epitaxial hybrid-heterojunction that contains a functional charged planar Te interlayer. Apart from the combined wide-bandgap of GaN and the narrow-bandgap of tellurium, the photoresponse of the heterojunction is also boosted by the charged planar Te interlayer due to the polarization charge on GaN surface, giving rise to a broadband light detection across the ultraviolet-infrared (UV-IR) spectrum (200–2500 nm). The samples are grown by physical vapor deposition (PVD), while the devices are fabricated by a shadow-mask-assisted electrode deposition technique, both in ultra-high vacuum (UHV) environment. The optoelectronic transport measurements confirm the self-powered broadband photodetection and synaptic behavior of paired-pulse facilitation (PPF). First-principles calculations reveal that the interfacial planar Te interlayer combined with spontaneous polarization of GaN modulated the electronic properties of the heterojunction, affecting carrier dynamics under light illumination. This work paves the way for the development of advanced photodetectors with applications in optoelectronics and neuromorphic computing.

1. Introduction

Wide-spectrum photodetection has garnered significant interest in various fields, such as optical communication [1–5], environmental monitoring [6], military [7], aerospace satellites [3], and biomedical imaging [8,9]. The traditional photodetectors typically target specific wavelength bands, limiting their utility for broadband detection [5,10,11]. Achieving a high-quality single broadband photodetection remains a significant challenge in material science and device engineering [4,12–14]. In recent years, researchers have turned to heterojunctions as a promising solution to modulate bandgaps effectively [15–19]. For example, wide-bandgap materials such as GaN [20], AlN, ZnO, and Ga_2O_3 are sensitive to ultraviolet light, while narrow-bandgap materials like PbS, PbSe, InSb, HgCdTe, Ge, and SiGe exhibit a strong response to infrared light [21]. To extend the range of detectable wavelengths, heterojunctions combining materials with different bandgaps have been proposed in various dimensional configurations [14,22]. Heterojunctions with mixed-dimensional materials, such as 0D/2D [23,24], 0D/3D [18], 1D/2D [25,26], 1D/3D [27], 2D/3D [22,28–30], and 0D/2D/3D [31–33], have demonstrated a broader wavelength range for effective photodetection.

In particular, the van der Waals (vdW) materials combined with 3D compounds have emerged as promising candidates for broadband photodetection due to their excellent optoelectronic properties [22]. In contrast to traditional materials, vdW heterostructures combine the distinctive properties of two-dimensional materials (also incorporate 1D materials through vdW interactions), such as large specific surface area [34] and the tunable bandgap [35,36], with the increasingly refined growth and device fabrication techniques of 3DMs [29]. This integration promises to enable the development of optoelectronic devices that are cost-effective, high-performance, low-power, and multifunctional. Despite these advancements, several key challenges remain in the fabrication of high-performance detectors, including understanding the underlying physical working mechanisms [37], optimizing device structures, and exploring the unconventional functionalities of vdW heterojunctions [15,29]. The three fundamental operating mechanisms

---

* Corresponding author.
E-mail address: yi.pan@xjtu.edu.cn (Y. Pan).

https://doi.org/10.1016/j.apsusc.2025.163492
Received 26 February 2025; Received in revised form 24 April 2025; Accepted 9 May 2025

of optoelectronic detectors have been widely studied [38,39]. These include: the photoconductive effect [28,30,40], wherein an applied bias separates photo-generated electron-hole pairs to extract current; the photovoltaic effect [5,22,41], where the built-in electric field at the junction surface separates electron-hole pairs; and the photo-gating effect [39], where photo-generated carriers are localized in states due to doping, defects, or bandwidth, acting as a local gate. The multifunctional operational mechanisms of photodetectors are further elucidated, such as the development of ultra-narrow band perovskite single crystals achieved through surface-charge recombination [42]. The charge collection narrowing mechanism is proposed, which can be realized by controlling the junction thickness [37,43]. Additionally, the charge separation reversion mechanism, which can be achieved by tuning the built-in electric field and the thickness, is presented for self-driven dual-band detection [19,44]. In particular, exploring the physical mechanisms underlying broadband detection in narrow- and wide-bandgap vdW heterojunctions, such as carrier dynamics, interfacial charge transfer, and band alignment, remains an urgent research problem yet to be fully addressed.

In this study, we propose a strategy for controlling the operation of self-powered broadband photodetectors based on polarization charge interlayer modulation at the heterojunction interface. This approach facilitates broadband (200–2500 nm) photodetection and has potential applications in neuromorphic computing. To realize this, we have employed physical vapor deposition (PVD) to fabricate a Te/GaN narrow/wide bandgap heterojunction, where the interface of the Te layer is influenced by the polarized substrate, leading to enhanced photodetection performance. The devices were fabricated using shadow mask-assisted electrode deposition in an ultra-high vacuum (UHV) environment. The optoelectronic transport measurements show that the device exhibits a response time of up to 600 ms for both infrared (IR) and visible (VIS) light, indicating its potential for applications in neuromorphic computing and brain-machine interfaces (BMI) [45–47]. Additionally, we performed first-principles calculations based on density functional theory (DFT) to conduct a comprehensive study of the heterojunction interface structure and electronic properties. Theoretical and experimental analyses reveal that the redistribution of the 2D electron gas (2DEG) at the interface under illumination alters the interface electric field, leading to the accumulation of charge carriers in the interface potential well, thereby enabling efficient photodetector operation [10]. Our findings provide new insight into the design of low-cost, high-performance, and multifunctional photodetectors, offering a promising direction for the future development of optoelectronic devices.

2. Method

2.1. Experimental details

Te films (~74 nm) were epitaxially grown on p-doped GaN(0001) substrates (4.5 ± 0.5 μm GaN on sapphire, Mg-doped, Suzhou Nanowin Science & Technology) in a custom ultra-high vacuum (UHV) chamber with a base pressure of 1×10^{-9} mbar. Prior to deposition, substrates underwent thermal degassing at 600 °C for 30 min. Tellurium was evaporated from a Knudsen cell containing 99.99 % purity Te powder (Alfa Aesar) at 283 °C, while maintaining the substrate temperature at 100 °C. Film growth proceeded for 15–20 min, followed by in situ post-annealing at the growth temperature for 30 min to optimize crystallinity.

Photoresponsive devices were fabricated using a multi-source UHV physical vapor deposition system (base pressure: 1×10^{-8} mbar). After removing the Te/GaN sample and installing the custom-designed shadow masks, the custom-shaped gold electrodes were deposited onto the Te/GaN in the vacuum chamber without the use of lithographic processing.

The sample surface morphology was analyzed using an optical microscope (OM) and a MIRA3-LMH scanning electron microscope (Tyco Electronics) operated at 15 kV. The morphology was further characterized using atomic force microscopy (AFM, Shimadzu SPM-9700HT) for nanoscale topography mapping, and Kelvin probe force microscopy (KPFM) with Au probes for surface potential profiling. Raman spectra were collected at room temperature using a confocal Raman spectrometer (HORIBA) equipped with a 532 nm laser (Renishaw InVia Qontor).

Electrical transport properties were characterized using a Keithley 2636B dual-channel source meter. A broadband Xe lamp (CME-SL300, Microenerg, 200–2500 nm) with bandpass filters provided wavelength-specific illumination (UV: 200–350 nm, VIS: 400–780 nm, IR: 780–2500 nm). Additional 1550 nm pulsed illumination was generated using a laser diode coupled to a programmable mechanical shutter (10 ms–10 s pulse width).

2.2. Calculational details

First-principles calculations were performed using the Vienna Ab Initio Simulation Package (VASP) [48] within the framework of density functional theory (DFT) employing a plane-wave basis set. The projector-augmented wave (PAW) [49] method was used to describe electron–ion interactions. At the same time, the Perdew-Burke-Ernzerhof (PBE) [50] functional within the generalized gradient approximation (GGA) [51] was applied to treat electron–electron interactions. Convergence criteria for atomic forces and total energy were set to 0.01 eV/Å and 1×10^{-4} eV, respectively. Energy cutoff values of 400 eV (Te/GaAs) and 550 eV (Te/GaN) were selected through convergence testing. The Brillouin zone was sampled using the Monkhorst-Pack scheme with a 5 × 5 × 1 k-point mesh for all 3 × 3 supercell structures. For GaAs(111) and GaN(0001), 13 × 13 × 1 and 9 × 9 × 1 k-point meshes were used, respectively. All models were constructed with a vacuum layer of approximately 20 Å to minimize interactions between periodic images. To simulate the bulk properties of the materials, the bottom six layers of the GaAs(111) and GaN(0001) substrates were passivated with 0.75 pseudo hydrogen atoms.

3. Results and discussion

3.1. Epitaxial growth of vdW Te on 3D GaN(0001) polar substrate

Fig. 1a illustrates the schematic diagram of the preparation of a Te/GaN heterostructure using PVD. In a vacuum environment, tellurium (Te) powder was directly evaporated from a Te source and deposited onto the surface of a p-GaN (0001) substrate, facilitating epitaxial growth of the Te film. This method eliminates the need for sample transfer, thereby avoiding oxidation and impurity adsorption during the transfer process, resulting in a high-quality heterostructure. The specific growth details are provided in the method section. Fig. 1b is a photograph of a 3 × 12 mm^2 heterojunction, showing a distinct Te nanolayer and clear boundaries on the substrate. The average thickness of the Te film is approximately 74 nm with a root-mean-square (RMS) roughness of about 6.27 nm, as shown in Fig. S1 and S2. Fig. 1c displays the typical Raman spectrum of the grown Te film under 532 nm laser excitation, featuring three distinct peaks at 94, 122, and 140 cm^{-1}, corresponding to the E^1, A^1, and E^2 modes, respectively. The A^1 vibrational mode is characterized as a chain expansion mode, where each atom oscillates within the basal plane of the lattice. In this mode, the collective atomic motions involve synchronous expansions and contractions along the plane. The E vibrational modes in the lattice primarily manifest as bond-bending around the direction perpendicular to the chain (E^1) and asymmetric bond-stretching types along the helical chain (E^2), with these characteristics being more pronounced in uniform thickness tellurium film [52,53].

We have conducted Raman spectroscopy measurements on the Te sample, focusing on six distinct points along the edge with varying thicknesses, as illustrated in the inset of Fig. 1c. As the thickness of the

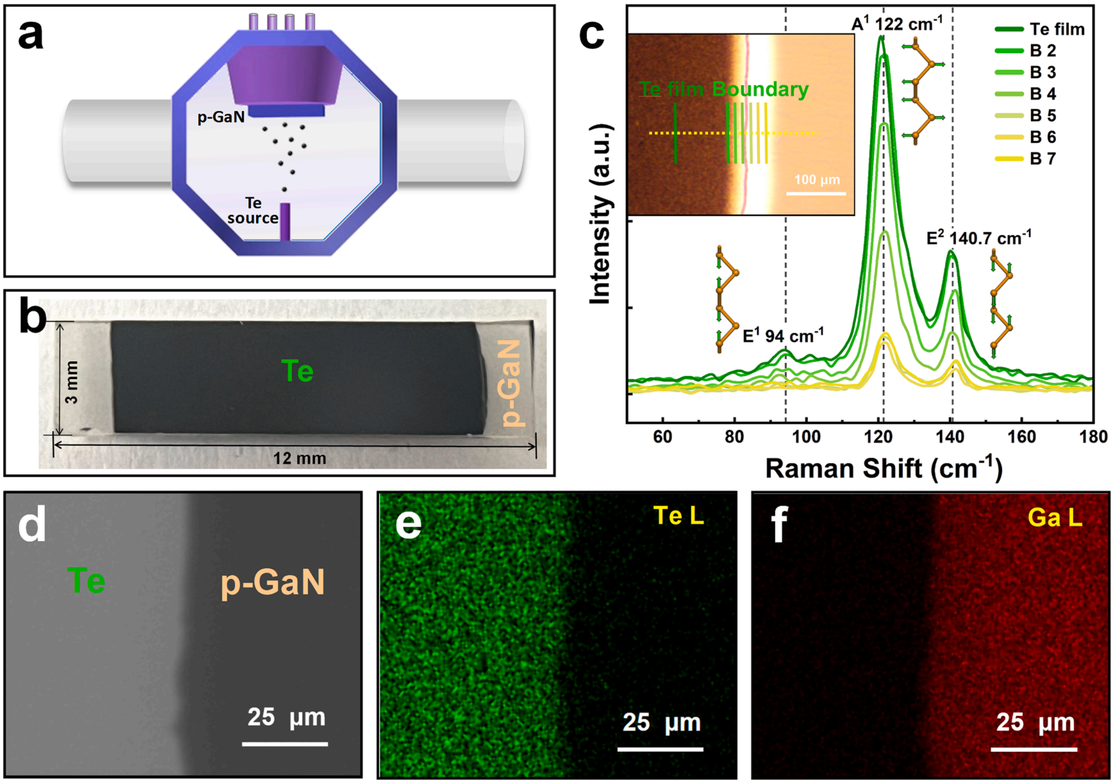

Fig. 1. (a) Schematic diagram illustrating the vdW Te nanosheets grown on p-GaN substrate by PVD. (b) Digital photograph of a Te/GaN 3 × 12 mm^2 sample. (c) Raman spectrum of Te nanofilm with different thicknesses at the boundary. The inset shows an optical microscopy image of the clean Te surface with the Te edge on the GaN. (d) SEM image of the Te edge on the GaN. (e-f) EDS elemental mapping of Te and Ga distributions in (d).

Te films decreased, we observed a progressive attenuation of the E^1 vibrational mode. In contrast, the A^1 and E^2 modes remained prominent, exhibiting slight blue shifts with reduced thickness. This observed trend is consistent with findings reported in the literature [53]. Additionally, we propose that the diminishment of the E^1 vibrational mode could be attributed not only to the vdW interactions that arise from the reduced film thickness and consequent electron overlap but also to the unique structural transition from the helical structure of the topmost layer to the planar Te of the bottom layer. This interface state of Te, characterized by its distinctive configuration, imposes constraints on atomic vibrations in the direction perpendicular to the Te chains. This alteration affects the electronic states, leading to the formation of a heterojunction transitional state.

We have performed scanning electron microscopy (SEM) analysis on the edge of the Te sample and energy-dispersive X-ray spectrometer (EDS) mapping to visualize the spatial distribution of Te and gallium (Ga) elements. The EDS mapping results revealed distinctly defined regions for Te and Ga, correlating with the respective locations of the Te film and the GaN substrate. Consequently, we obtained narrow- and wide-bandgap Te/GaN van der Waals heterojunction samples for device fabrication.

3.2. *Self-powered broadband photodetector (PD) fabricated on Te/GaN*

We employed a home-built multi-source stencil lithography system to deposit Au electrodes onto the sample surface in UHV. The electrode patterns were created using custom-designed metal shadow masks, as illustrated in Fig. 2a. The red dashed box in Fig. 2a highlights the specific area observed under SEM, revealing distinct rectangle-shaped Au electrodes on the surface of the Te/GaN heterostructure (Fig. 2b). A magnified view of the corner edge of the Au electrode is shown in Fig. 2c, where EDS analysis was performed to obtain detailed insights into the photodetector's structural composition (Fig. 2e-f). Fig. 2d presents a schematic diagram illustrating the structure of the Te/GaN heterojunction PD. We successfully fabricated vertical photodetectors with gold electrodes based on Te/GaN narrow- and wide-bandgap heterojunctions designed for broadband optical detection.

As shown in Fig. 2g, we have measured the typical current–voltage (*I-V*) characteristics of the photodetector. Upon illumination, the device demonstrates a self-powered photovoltaic effect, generating a photocurrent without external bias. The photocurrent response is most pronounced under UV illumination, while reasonably high photocurrents are observed under VIS and IR light. Under UV–VIS-IR illumination, the magnitude of the interface electric field is influenced by the dynamics of photogenerated carriers' generation, separation, and transport at different wavelengths, which is explained in detail in Section 3.4. It provides valuable insight into the device's optoelectronic response and potential for broad-spectrum photodetection.

The broad-spectrum photodetection capability of the Te/GaN PD can chiefly be attributed to the strategic selection of wide-bandgap 3D GaN and narrow-bandgap vdW material Te. The unique optical response and its applications are primarily driven by the interfacial electronic properties of the heterojunction and the distinctive interface structure of Te. Fig. 2g-h illustrate the band structures and electronic density of states (DOS) of bulk GaN and Te, calculated using the VASP software. Although the bandgap values are underestimated due to the known limitations of the GGA-PBE approximation, the results clearly imply that the direct bandgap of GaN is significantly larger than that of direct bandgap Te by more than an order of magnitude. The direct bandgap facilitates efficient electron transitions and high absorption efficiency.

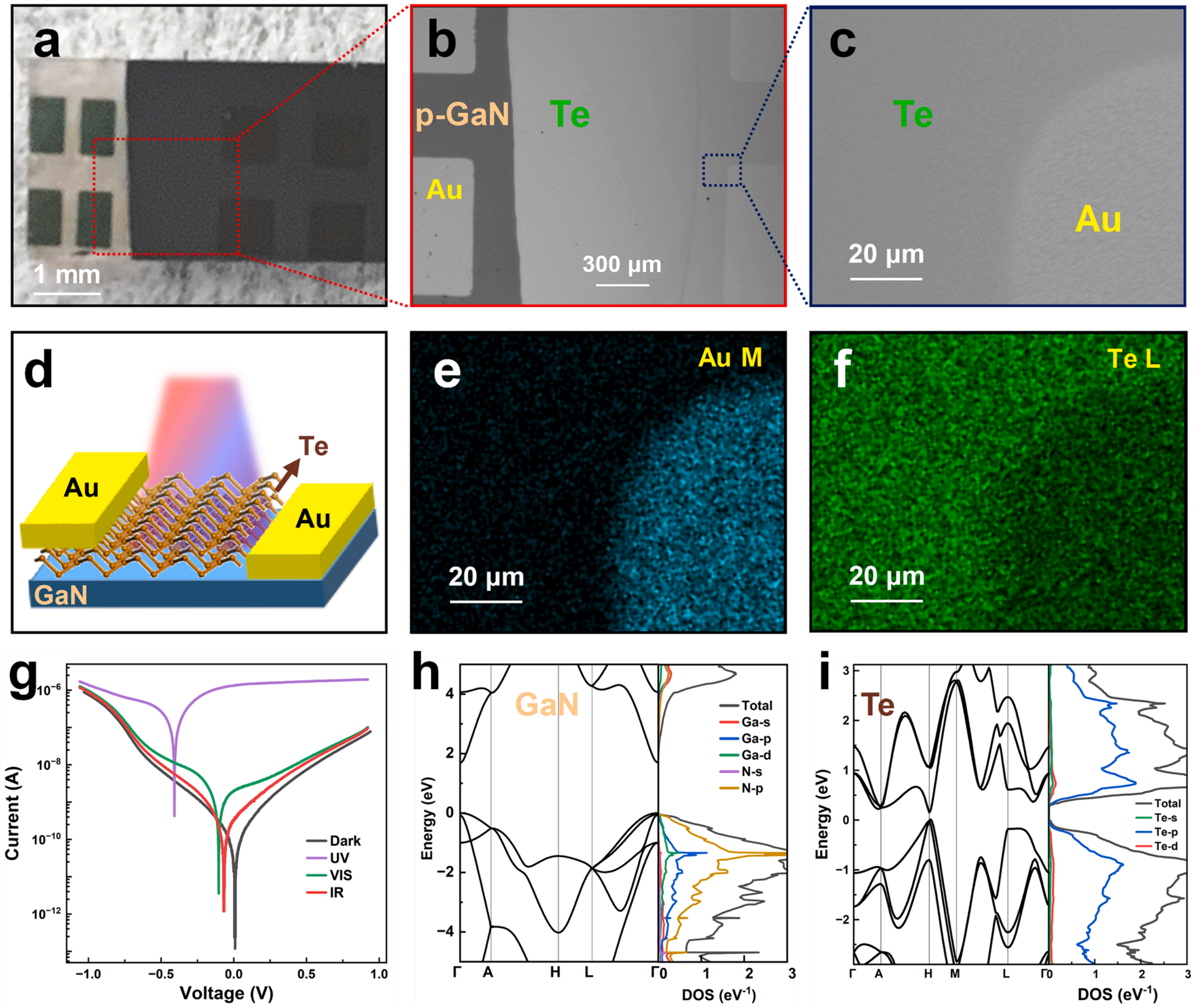

Fig. 2. (a) Photograph of the Te/GaN PD device. (b) SEM image of the Te edge on the GaN with Au electrodes in the area enclosed by the red rectangular in (a). (c) Zoom-in SEM image of an Au electrode boundary on continuous Te film. (d) Schematic of the Te/GaN photodetector (PD) device with Au metal electrodes. (e-f) EDS elemental mapping of Au and Te distributions in the blue rectangle in (b). (g) Logarithmic plot of *I-V* curve of the Te/GaN photodetector obtained in the dark (dark line) and under the illumination of constant light power intensity with bandpass filters for infrared (red line), visible (green line), and ultraviolet (purple line) light. (h-i) Energy bands and electronic density of states (DOS) of (h) GaN and (i) Te calculated by DFT. (For interpretation of the references to colour in this figure legend, the reader is referred to the web version of this article.)

The electronic states near the band edges for both materials are predominantly composed of p-orbital contributions. The unique interface behavior of the heterostructure further amplifies the photodetector's response, highlighting its potential for advanced optoelectronic applications, such as environmental monitoring and night vision imaging.

3.3. *PD performance with broadband synaptic photoresponse*

We have measured the photoresponse performance of the Te/GaN photodetector with pulsed light of varying wavelengths. Under zero external bias, the photocurrent generated by light pulses (pulse width of 4 s) of UV (200–350 nm), VIS (400–780 nm), and IR (780–2500 nm) (Different wavelengths were obtained through bandpass filters from a continuous-wavelength Xe lamp light source) as a function of time t is shown in Fig. 3a-c, respectively. The rise and decay times of the Te/GaN device under UV, VIS and IR light irradiation are presented in Fig. S4. As the optical power density (P) increases, the induced current rises, reaching the micro ampere range for UV illumination and the nano ampere range for VIS and infrared IR light. The dark current (I_{off}) of photodetectors is measured in a dark box without illumination. Thus, the current mainly originates from thermally generated carriers and intrinsic noise within the material. The on/off ratio of the device, defined as the ratio of photocurrent under illumination to dark current, is directly dependent on the responsivity. In our fabricated Te/GaN photodetector, the dark current is below 0.5 pA. Under UV illumination at an intensity of 12.5 mW/cm^2, the on/off ratio reaches 10^6, demonstrating a highly sensitive response. Meanwhile, under the illumination intensity of 27 mW/cm^2 in the VIS and IR ranges, the on/off ratio achieves 10^3.

The linear relationship between photocurrent ($I_{ph} = I_{lig} - I_{off}$) and incident light power density (*P*) under illumination (UV, VIS, and IR) is shown in Fig. 3d. Here, I_{ph} and *P* can be described by a power function fit, $I \propto AP^{\alpha}$, where the fitting constant A represents the response intensity of the device at a specific wavelength, and α is the fitting exponent. A higher α value indicates a greater sensitivity of the photodetector to variations in light intensity, resulting in a more considerable output change in photocurrent. However, a higher α does not necessarily imply an increase in responsivity. Under UV illumination, the exponent α is

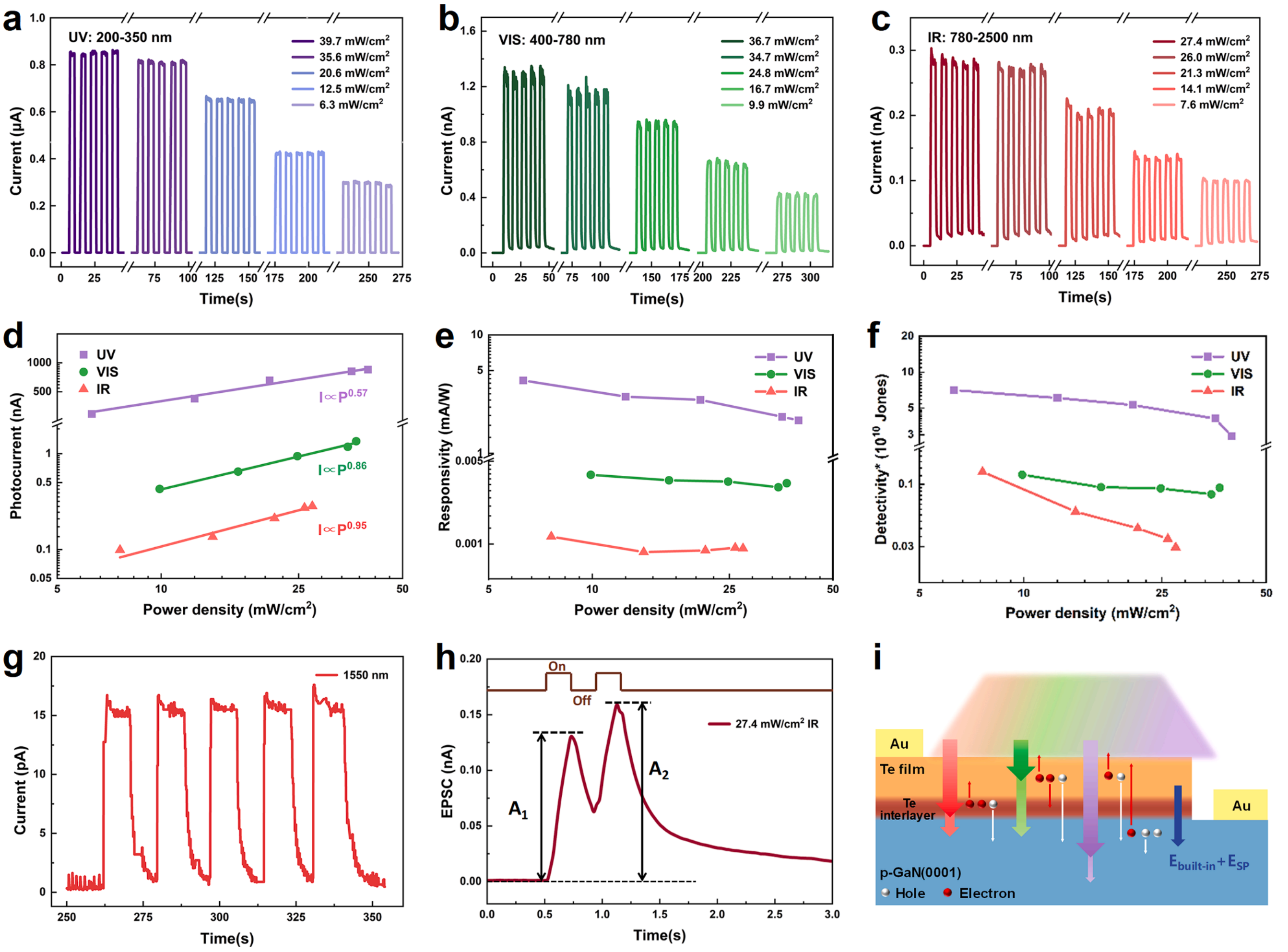

Fig. 3. (a-c) Self-powered (zero bias) I-t curves obtained under shutter-controlled pulsed Xe lamp light illumination of different wavelength ranges, (a) $\lambda = 200-350$ nm, (b) $\lambda = 400-780$ nm, (c) $\lambda = 780-2500$ nm. (d) Photocurrent, (e) responsivity, and (f) detectivity (D*) as a function of the power density of the PD for the light of various wavelengths. (g) Self-powered I-t curve for 1550 nm light illumination. (h) PPF behavior triggered by two consecutive shutter-controlled light pulses ($t_p = \Delta t = 0.2$ s). (i) Schematic diagram of the Te layer at the Te/GaN detector interface that binds the carriers and delays the response time under illumination.

0.57, while it increases to 0.86 for VIS light and reaches 0.95 for IR light. The progressively larger α values with longer wavelengths suggest enhanced sensitivity to light intensity changes in the IR range. With $\alpha \approx 1$ under IR illumination, the device exhibits an almost linear response and closely approaches the characteristics of an ideal linear photodetector. The intercept on the vertical axis represents the dark current, which is crucial for evaluating the signal-to-noise ratio (SNR) and performance under low light conditions. The variation in dark current observed under different illumination wavelengths is primarily attributed to factors such as material absorption coefficient, defect state activation, surface state effects, and thermal impacts [54]. For example, ultraviolet light can induce significant band-to-band transitions, leading to an increased generation of photocarriers that elevate the “background” component of the dark current. In contrast, IR light has a relatively minor impact (Table S1).

Based on the measured photocurrent values and the effective excitation area of the device, we calculated the key performance parameters of the Te/GaN photodetector, plotting the responsivity and detectivity (D*) as functions of light power density (P) across UV, VIS, and IR wavelengths in Fig. 3e–f (calculation details are provided in the Electronic Supplementary Material). In Fig. 3e, UV light demonstrates a relatively higher response of 4.1 mA/W under 6.3 mW/cm^2, indicating enhanced sensitivity to UV light due to more efficient photon absorption and carrier generation. In contrast, under longer-wavelength VIS and IR illumination, the lower-energy photons lack sufficient energy to excite electrons across the 3.4 eV bandgap of GaN, leaving only Te, with its narrow 0.3 eV bandgap, to contribute to the photoresponse. Consequently, the responsivities under VIS and IR illumination are relatively lower, reaching the few hundred picoampere level at 10 mW/cm^2. In Fig. 3f, the detectivity under UV illumination remains relatively high, reaching up to 7×10^{10} Jones at 6.3 mW/cm^2. This highlights the photodetector’s superior performance in detecting low-intensity UV signals with minimal noise contributions. Under VIS and IR illumination, however, the photodetector’s performance is affected by factors such as thermal noise, photogenerated carrier noise, and electronic noise. For instance, infrared photons have relatively low energy but intense penetration, allowing them to reach deeper layers of the material, which leads to an overall temperature increase and generates thermal noise. We measured the detectivity of the Te/GaN photodetector at room temperature in ambient pressure, where background radiation noise and thermal noise unavoidably impact the detection of low-intensity and distant infrared signals, potentially underestimating the signal-to-noise ratio (SNR) and detectivity. Under these conditions, we measured a detectivity of 10^9 Jones at 7.6 mW/cm^2 VIS and IR illumination for the Te/GaN photodetector. These results demonstrate that the epitaxially grown vdW Te/GaN heterostructure device exhibits superior photoresponse performance compared to other Te-based photodetectors [55–57].

In particular, the PD shows prominent IR response up to the wavelength of 1550 nm, as measured with a laser diode light source. The

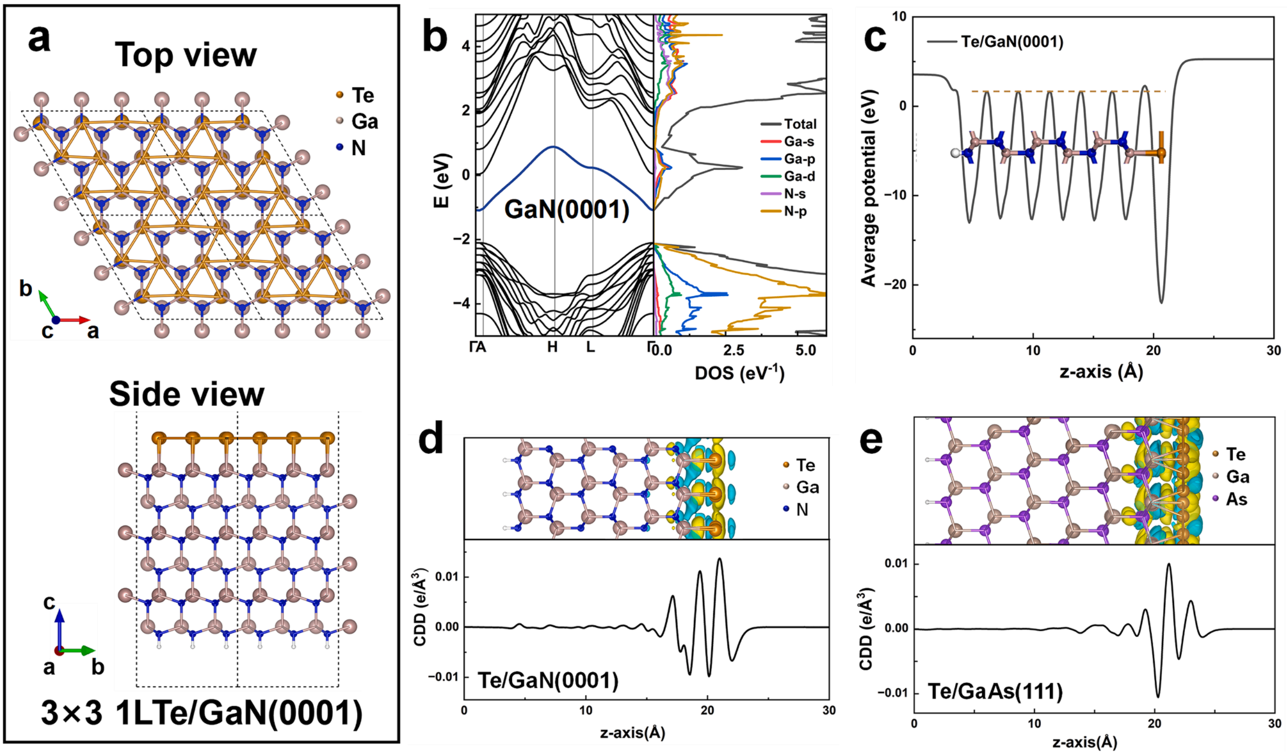

Fig. 4. (a) The atomic structure model of 3 × 3 monolayer Te/GaN(0001). (b) The band structure and DOS of GaN(0001) with a new energy level near the Fermi surface (blue band line). (c) The average potential energy change of Te/GaN(0001) along the z-direction. (d-e) Comparison of the charge density difference (CDD) of the monolayer Te on the surface of (d) GaN(0001) and (e) GaAs(111). The yellow and cyan areas correspond to charge accumulation and depletion, respectively. (For interpretation of the references to colour in this figure legend, the reader is referred to the web version of this article.)

detector exhibits a photocurrent response of 15 pA under 4.6 mW/cm^2 infrared pulsed illumination, with the current–time relationship shown in Fig. 3g. It is observed that the decay time is significantly longer than the rise time, a trend consistently evident across multiple spectral bands in Fig. 3a–b. Notably, under IR and VIS illumination, the response time reaches approximately 600 ms, whereas the rise and decay times under UV illumination are only around 100 ms. (The response time is influenced by factors such as light power density, wavelength, pulse count, and pulse frequency. Detailed response times across different spectral bands are provided in Fig. S4.) Furthermore, under VIS and IR light, the decay time is prolonged with cumulative pulsing, as illustrated in Fig. 3b-c. Unlike applications that require rapid response times, such as photodetection and optical communication, the essence of memory in neuroscience and artificial intelligence lies in repetition. Synaptic connections between neurons are altered through repeated activation and stimulation, which plays a critical role in memory formation and maintenance. In this context, the extended decay times observed in Te/GaN PD, caused by the interface characteristics, provide a distinct advantage for simulating short-term plasticity (STP) in neuromorphic applications. We performed paired-pulse facilitation (PPF) tests under infrared illumination, with the results presented in Fig. 3h. PPF describes the response variation in synaptic transmission under consecutive pulse stimulations, characterized by excitatory postsynaptic current (EPSC). Two pulses, each with a width of 200 ms, were applied with a 200 ms interval, approximately 33 % of the infrared decay time. The PPF index (defined as A_1/A_2) was calculated as 1.22, exceeding 1. This is because the second pulse accumulates the carriers released from the interface trap states during the decay time of the first pulse, resulting in an enhanced current response. Therefore, the second infrared pulse induces an enhanced synaptic-like response.

The Te/GaN photodetector exhibits differential responses across multiple spectral bands, with prolonged response times under VIS and IR illumination due to carrier trapping and accumulation, as illustrated in Fig. 3i. This effect arises from the interface Te layer, which is influenced by the polar GaN(0001) substrate and forms a potential well that traps carriers at the interface. The polar charges at the interface exhibit different distributions under varying illumination conditions, altering the interfacial electric field and affecting the decay time of the Te/GaN photodetector. The subsequent section provides a comprehensive explanation of the underlying operational mechanisms of the detector.

3.4. Photoresponse mechanism elucidated by first-principles calculations

To elucidate the photoresponse mechanism of the Te/GaN PD, the heterojunction was simplified as an interfacial system between the 3D GaN (GaAs) substrate and van der Waals (vdW) Te for DFT calculations. We constructed a six-bilayer 3 × 3 GaN(0001) substrate ($a = 3.22$ Å) to calculate the electronic states at both the substrate surface and heterojunction interface. Based on the optimized Te-Te bond length of 2.90 Å and the preferred Ga atop adsorption site for a single Te atom, a Te layer was placed atop each Ga atom on the GaN(0001) surface for structural relaxation.

As shown in Fig. 4a, the fully relaxed configuration reveals that Te atoms form covalent bonds with Ga atoms, creating a flat Te layer. For comparison, a Te atomic layer was placed directly above the Ga atoms on a GaAs(111) surface ($a = 4.07$ Å), forming a flat yet stepped Te chain structure (Fig. S5). This difference arises because GaAs have a larger lattice constant than GaN, increasing the stretching distance during bonding and reducing the connectivity of the Te atoms. On GaN(0001), each Te atom forms bonds with five neighboring atoms in a net structure, while on GaAs(1 1 1), each Te atom forms three bonds, leading to a less interconnected arrangement. Upon removal of the GaN and GaAs substrates, the flat Te layer, unaffected by the substrates, tends to recover its intrinsic helical chain configuration and transforms into a structure characterized by helical-like chains (details provided in the Electronic Supplementary Material). It is confirmed that Te undergoes

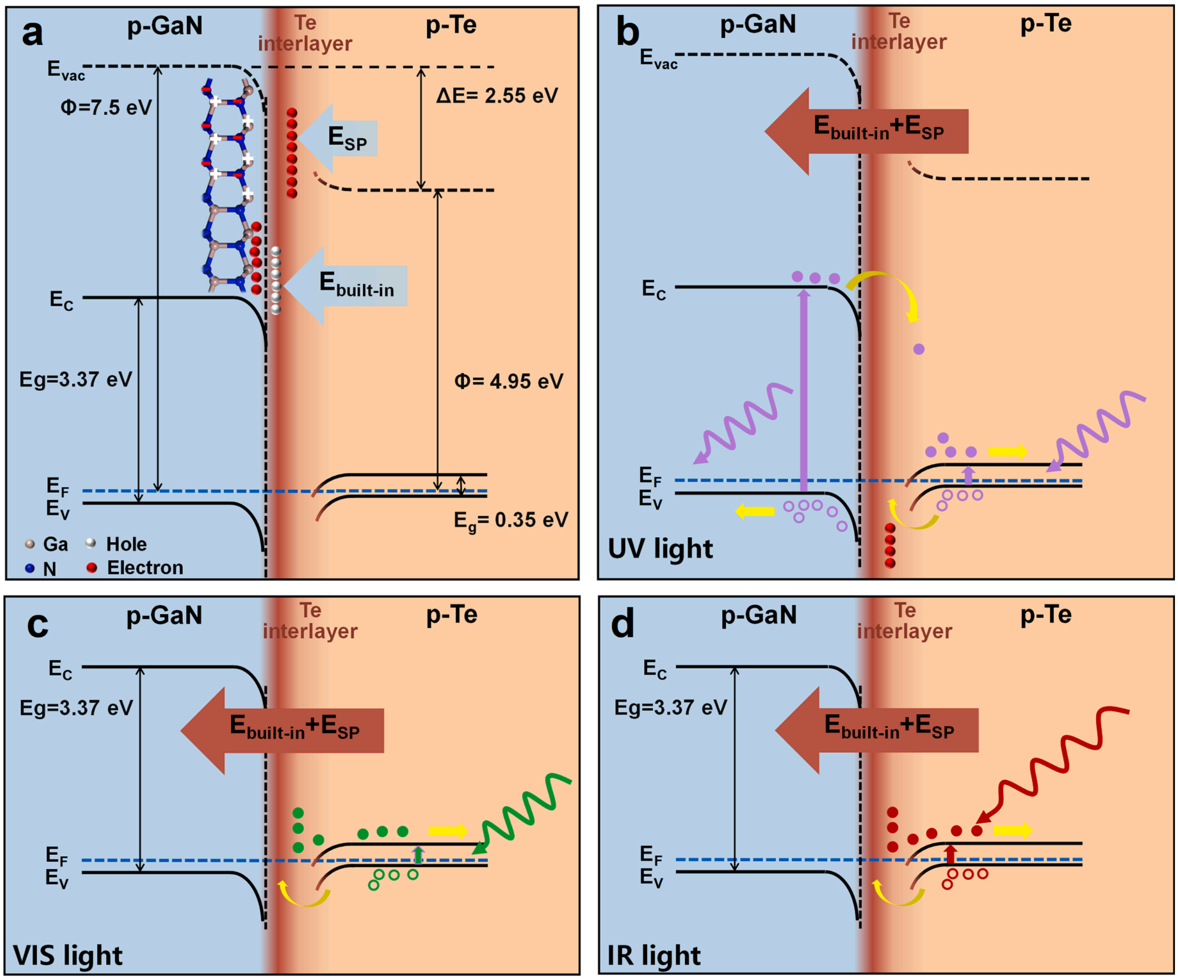

Fig. 5. The band alignment of Te and GaN(0001). The photoresponse mechanism of PD under (a) dark, (b) UV, (c) VIS and (d) IR light condition.

surface reconstruction on GaN(0001), forming a planar Te buffer layer that minimizes interfacial defects while serving as an intermediate layer bridging the wide-narrow bandgap transition (Fig. S6).

Fig. 4b presents the band structure and density of states (DOS) for GaN(0001), where the primary electronic states arise from the p orbitals of N and Ga atoms. Unlike bulk GaN (Fig. 2h), an additional interface-induced energy level appears at the conduction band minimum, with a significantly increased contribution from the p orbitals of Ga atoms. This newly formed interface band aligns with previous reports in the literature [58]. It synergistically couples with the narrow-bandgap Te layer to mitigate abrupt bandgap variations at the heterointerface. Fig. 4c shows the average potential profile of the Te/GaN(0001) heterojunction along the z-axis. The periodic oscillations observed in the plot typically correspond to the presence of atomic layers within the heterostructure, where each potential valley indicates the low-potential region surrounding an atomic nucleus. The valleys in the Te layer are noticeably lower than those in the GaN layer, reflecting differences in their crystal structures and electronic distributions. At the Te/GaN interface, a sharp potential well is observed, suggesting the presence of an intrinsic electric field introduced by the interface. Additionally, the GaN(0001) surface is inherently polar, further affecting the distribution of interfacial charges. This polarization and built-in electric field play a crucial role in the heterojunction’s conductive properties and the formation of a 2DEG at the Te interlayer, which is critical for potential electronic and optoelectronic applications [59]. Whether the bonding of additive molecules on the perovskite surface induces sub-bandgap trap states also is an interface issue of concern for the performance of inverted solar cells [60].

We conducted differential charge density mapping for the Te/GaN (0001) heterojunction, as shown in Fig. 4d, and calculated a similar differential charge density map for Te/GaAs(111) (Fig. 4e) for a comparative study to investigate the impact of spontaneous polarization on interfacial charge distribution. In both cases, the Ga atomic layer on the substrate surface exhibits an electron depletion of approximately 0.005 e/Å^3. In comparison, the covalent bond layer between the Te atomic layer and the substrate shows an electron accumulation of 0.01 e/Å^3. However, there is a notable difference in the electron accumulation on the Te layer. On the GaN substrate, the Te atomic layer accumulates over 0.01 e/Å^3, which is more than twice the electron gain observed on the Te layer on the GaAs substrate. Such a discrepancy arises from the spontaneous polarization in GaN, which drives charge accumulation on the flat Te layer, forming 2DEG and effectively modulating the interfacial electric field.

We analyzed the band alignment to explore the photoresponse mechanism in the Te/GaN heterojunction device, considering its transmission and absorption characteristics across the UV–VIS-IR spectrum (Fig. S7). The *I-V* curve reveals that Te forms an Ohmic contact with the Au electrode (see Fig. S8), confirming that the undoped Te film exhibits p-type conductivity, thereby establishing a p-Te/p-GaN heterojunction. Before contact, the work function of p-Te is 4.95 eV [55,61], which is lower than that of p-GaN at 7.5 eV [62]. The work function difference of the Te/GaN heterojunction is 2.55 eV, which is close to the potential difference of 2.48 eV obtained from the KPFMcharacterization results (Fig. S3). Consequently, the Fermi level of Te is higher than that of GaN, prompting electron diffusion from Te to GaN. Upon contact, the Fermi levels of the two semiconductors align, establishing a thermodynamic equilibrium, and a straddling gap (Type I) heterojunction is formed [63]. A built-in electric field ($E_{\text{built-in}}$) is formed pointing from Te towards GaN. At this point, the band edges of GaN bend downward, while those of Te bend upward. The spontaneous polarization of GaN(0001) introduces polarization charges accumulation at the Te film interface (forming 2DEG), leading to additional downward bending of the band edges (Fig. 5). The downward-bending band edges at both sides of the heterojunction interface are asymmetric, with the GaN(0001) band dropping steeply, while the band edge on the Te film side decreases more gradually. This creates an interface potential well. The interfacial polarization field, directed from Te toward GaN (With the Ga-face oriented towards the Te film, the polarization direction is along the (0001) crystallographic axis), effectively enhances the strength of the $E_{\text{built-in}}$ (Fig. 5a). As a result, the interfacial field strength is the combined effect of the $E_{\text{built-in}}$ and the spontaneous polarization field (E_{sp}).

Under UV illumination, the bulk GaN substrate provides more efficient photon adsorption (Fig. S7), which gives rise to a strong photoresponse (Fig. 5b). The photogenerated electrons in GaN move toward the Te film under the interface electric field. In contrast, photogenerated holes are transported to the Au electrode, enabling the separation of photogenerated carriers. A portion of the photogenerated holes accumulate at the interface, in collaboration with the polarized positive charges in GaN, attract more electrons to accumulate at the Te film interface, lowering the Te conduction band and enhancing the interface electric field. This enhanced interface field further facilitates the separation of photogenerated carriers, preventing recombination of photogenerated holes with polarization charges at the Te film interface. Thus, the amplified interface electric field under UV illumination significantly contributes to the intense UV photoresponse of the Te/GaN heterojunction PD (Fig. 2g).

Under IR and VIS illumination, only Te generates photogenerated electrons and holes (Fig. 5c, d). The rise time of the photoresponse is determined by the speed at which carriers reach saturation value, while the decay time is influenced by the trapping effect of accumulated carriers. The Te film exhibits a lower transmittance rate for IR light compared to VIS light, resulting in higher absorption (Fig. S7). Due to the lower energy of IR photons, they penetrate deeper, leading to a large generation of photogenerated carriers at the Te film interface in the heterojunction (Fig. 5d). Under the effect of the interface electric field, the majority of photogenerated holes cross the interface barrier and move toward GaN (Some photogenerated holes neutralize the polarization charges). The photogenerated electrons, in addition to being trapped by the interface potential well which increases the decay time of the photoresponse (Fig. 3c, g, Fig. S4c), also participate in the polarization charge at the Te film interface, slightly enhancing the interface electric field. However, a disadvantage is that the carriers need to travel a long distance from the heterojunction interface to the Au electrode, leading to a high recombination rate and a low response rate (Fig. 2g, Fig. 3c, d).

VIS light has a lower absorption and penetration depth, which results in the generation of photogenerated carriers at the surface of the Te film (Fig. S7). The photogenerated electrons are rapidly captured by the Au electrode, while some diffuse with the photogenerated holes to the heterojunction interface (Fig. 5c). The interface potential well traps the photogenerated electrons, and then, under the interface electric field, they return to the Te film, extending the carrier lifetime and decay time (Fig. 3b, Fig. S4b). Photogenerated electrons also participate in interface charge accumulation, enhancing the electric field and promoting carrier separation.

Therefore, under UV illumination, the significantly enhanced interface electric field effectively drives carriers to the Au electrode, resulting in the shortest decay time for the Te/GaN photodetector, reaching only a hundred milliseconds (Fig. S4). In contrast, the response of PD to VIS and IR light exhibits decay times extending to several hundred milliseconds (Fig. S4). The performance comparison of the Te/GaN device with other similar-type devices is shown in Table S2 and S3.

4. Conclusion

In summary, the hybrid-heterojunction between the vdW narrow-bandgap Te and 3D wide-bandgap GaN was grown via PVD under ultra-high vacuum, ensuring an ultraclean interface and flat surface growth, confirmed by OM, AFM, KPFM, Raman spectroscopy, SEM, and EDS. The Te/GaN photodetector, with Au electrodes deposited using a custom-patterned metal shadow mask, exhibits stable self-powered broadband photoresponse from 200 to 2500 nm. This device performs a UV response time of ~ 100 ms, significantly faster than the ~ 600 ms response for VIS and IR light. This discrepancy arises from the spontaneous polarization of GaN(0001), where the polarization field dynamically modulates the interface electric field through charge redistribution at the wide- and narrow-bandgap heterojunction interface under varying illumination conditions, thereby affecting carrier separation efficiency. The mechanism was further confirmed by first-principles calculations, which show that the Te layer forms a flat structure on the substrate surface, accumulating a significant amount of 2DEG at the interface. At the heterojunction interface, the Te interlayer acts as a buffer layer that regulates the photoresponse time. Our study provides new material options and insights into the working mechanisms for the development of broadband optical detection, imaging, environmental monitoring, and other applications.

CRediT authorship contribution statement

Wenmin Li: Writing – original draft, Investigation, Data curation. **Yongqi Hu:** Validation, Data curation. **Xutao Zhang:** Validation, Data curation. **Hao Hu:** Methodology, Conceptualization. **Yi Pan:** Writing – review & editing, Supervision, Resources, Project administration, Methodology, Funding acquisition, Conceptualization.

Declaration of competing interest

The authors declare that they have no known competing financial interests or personal relationships that could have appeared to influence the work reported in this paper.

Acknowledgments

This work was financially supported by the National Key Research and Development Program of China (Grant no. 2022YFA1204100), the National Natural Science Foundation of China (Grant no. 12074302), and the Strategic Priority Research Program of the Chinese Academy of Sciences (Grant no. XDB30000000).

Appendix A. Supplementary material

Supplementary material (the details of the optical response measurements and calculations of the Te/GaN photodetector, as well as the first-principles calculations of the heterojunction, are presented.) is available in the online version of this article. Supplementary data to this article can be found online at https://doi.org/10.1016/j.apsusc.2025.163492.

Data availability

Data will be made available on request.

References

[1] J. Liu, J. Jiang, S. Wang, T. Li, X. Jing, Y. Liu, Y. Wang, H. Wen, M. Yao, X. Zhan, L. Shen, Fast response organic tandem photodetector for visible and near-infrared digital optical communications, Small 17 (2021) e2101316.

[2] L.H. Zeng, S.H. Lin, Z.J. Li, Z.X. Zhang, T.F. Zhang, C. Xie, C.H. Mak, Y. Chai, S. P. Lau, L.B. Luo, Y.H. Tsang, Fast, self-driven, air-stable, and broadband

photodetector based on vertically aligned $PtSe_2$/GaAs heterojunction, Adv. Funct. Mater. 28 (2018) 1705970.
[3] S.A. Stankevich, Evaluation of the spatial resolution of digital aerospace image by the bidirectional point spread function parameterization, Mathematical Modeling and Simulation of Systems (MODS'2020) (2021) 317–327.
[4] Y. Pan, X. Wang, D. Zhang, Z. Wei, Y. Xu, Y. Li, Q. Li, Z. Zhao, Z. Zhu, B.S. Bae, D. C. Onwudiwe, X. Xu, W. Lei, Visible elimination, ultraviolet and near-infrared dual-band photodetector based on single-crystal perovskite heterojunctions toward secure optical communication, ACS Photonics 11 (2024) 1252–1263.
[5] M. Li, J. Xu, K. Zhu, S. Shi, Q. Zhang, Y. Bu, J. Chen, J. Xu, Q. Zheng, Y. Su, X. Zhang, L. Li, The fabrication of a self-powered $CuInS_2/TiO_2$ heterojunction photodetector and its application in visible light communication with ultraviolet light encryption, J. Mater. Chem. C 9 (2021) 14613–14622.
[6] X. Zhang, J. Zhao, X. Fu, Y. Lin, Y. Qi, H. Zhou, C. Zhang, Broadband vibration energy powered autonomous wireless frequency monitoring system based on triboelectric nanogenerators, Nano Energy 98 (2022) 107209.
[7] S. Das, K.J. Sarkar, B. Pal, H. Mondal, S. Pal, R. Basori, P. Banerji, SnS_2/Si nanowire vertical heterostructure for high performance ultra-low power broadband photodetector with excellent detectivity, J. Appl. Phys. 129 (2021) 053105.
[8] S. Kim, Y.T. Lim, E.G. Soltesz, A.M. De Grand, J. Lee, A. Nakayama, J.A. Parker, T. Mihaljevic, R.G. Laurence, D.M. Dor, L.H. Cohn, M.G. Bawendi, J.V. Frangioni, Near-infrared fluorescent type II quantum dots for sentinel lymph node mapping, Nat. Biotechnol. 22 (2004) 93–97.
[9] F.C. Lussani, R.F. Vescovi, T.D. de Souza, C.A. Leite, C. Giles, A versatile x-ray microtomography station for biomedical imaging and materials research, Rev. Sci. Instrum. 86 (2015) 063705.
[10] B. Jo, K. Seo, K. Park, C. Jeong, B. Poornaprakash, M. Lee, S. Ramu, M.G. Hahm, Y. L. Kim, Trap-assisted monolayer $ReSe_2$/Si heterojunction with high photoconductive gain and self-driven broadband photodetector, Front. Mater. 11 (2024) 1354522.
[11] W. Cheng, W. Tian, F. Cao, L. Li, Self-powered bifunctional perovskite photodetectors with both broadband and narrowband photoresponse, InfoMat 4 (2022) e12348.
[12] J. Zhang, W. Wang, H. Ye, R. Huang, C. Liu, W. Zhao, Y. Shi, Ultra-broadband ultraviolet–visible light–short wavelength infrared InGaAs focal plane arrays via n-InP contact layer removal, Sensors 24 (2024) 1521.
[13] Y. Yang, X. Liu, T. Liu, D. Chen, Z. Ye, J. Li, Q. Huang, Y. Zhu, Y. Pang, D. Zhang, Z. Liu, B. Cheng, J. Zheng, Y. Zuo, High-speed broadband hybrid perovskite nanocrystals /Ge photodetector from UV to NIR, Adv. Opt. Mater. 11 (2023) 2300708.
[14] J. Yao, G. Yang, 2D material broadband photodetectors, Nanoscale 12 (2020) 454–476.
[15] Z. Li, M. Zhang, Z. Fu, Z. Zhang, S. Wu, Y. Zhang, D. Lin, R. Hong, J. Cai, X. Chen, F. Zhang, Poly-Si/a-Si/4H-SiC p-n heterojunction broadband photodetector prepared by magnetron sputtering, J. Phys. D Appl. Phys. 57 (2024) 215108.
[16] Q. Fan, H. Zhang, K. Li, Z. Jin, T. Zhang, C. Wan, X. Liu, S. Li, J. Huang, Narrowband and broadband dual-mode perovskite photodetector for RGB detection application, Adv. Opt. Mater. 11 (2023) 2300272.
[17] F. Yıldırım, E. Bacaksız, A. Türüt, Ş. Aydoğan, Self-driven, stable broadband photodetector based on GaAs:CdS heterojunction with ultrahigh on/off ratio and detectivity, Surf. Interfaces 44 (2024) 103709.
[18] R. Meng, Z. Qiao, Q. Jiang, D. Liu, Efficient heterojunction constructed from wide-bandgap and narrow-bandgap small molecules enables dual-band absorption transparent photovoltaics, J. Mater. Chem. A 11 (2023) 26212–26220.
[19] Y. Li, F. Guo, S. Yu, J. Wang, S. Yang, Bipolar dual-broadband photodetectors based on perovskite heterojunctions, Nano Futures 6 (2022) 025006.
[20] D. Guo, Y. Su, H. Shi, P. Li, N. Zhao, J. Ye, S. Wang, A. Liu, Z. Chen, C. Li, W. Tang, Self-powered ultraviolet photodetector with superhigh photoresponsivity (3.05 A/W) based on the GaN/Sn:Ga_2O_3 pn junction, ACS Nano 12 (2018) 12827–12835.
[21] A. Rogalski, J. Antoszewski, L. Faraone, Third-generation infrared photodetector arrays, J. Appl. Phys. 105 (2009) 091101.
[22] Z. Zeng, D. Wang, X. Fang, C. Zhao, B. Zhang, D. Liu, T. Chen, J. Pan, S. Liu, G. Liu, T. Liu, H. Jin, S. Jiao, L. Zhao, J. Wang, Self-powered broadband photodetector based on Bi_2Se_3/GaN pn mixed-dimensional heterojunction with boosted responsivity, Mater. Today Nano 23 (2023) 100372.
[23] Z. Ni, L. Ma, S. Du, Y. Xu, M. Yuan, H. Fang, Z. Wang, M. Xu, D. Li, J. Yang, W. Hu, X. Pi, D. Yang, Plasmonic silicon quantum dots enabled high-sensitivity ultrabroadband photodetection of graphene-based hybrid phototransistors, ACS Nano 11 (2017) 9854–9862.
[24] G. Kara, P. Rohner, E. Wu, D.N. Dirin, R. Furrer, D. Poulikakos, M.V. Kovalenko, M. Calame, I. Shorubalko, Scaling of hybrid QDs-graphene photodetectors to subwavelength dimensions, ACS Photonics 11 (2024) 2194–2205.
[25] J. You, Z. Jin, Y. Li, T. Kang, K. Zhang, W. Wang, M. Xu, Z. Gao, J. Wang, J.K. Kim, Z. Luo, Epitaxial growth of 1D Te/2D $MoSe_2$ mixed-dimensional heterostructures for high-efficient self-powered photodetector, Adv. Funct. Mater. 2311134 (2023).
[26] J.-J. Tao, J. Jiang, S.-N. Zhao, Y. Zhang, X.-X. Li, X. Fang, P. Wang, W. Hu, Y. H. Lee, H.-L. Lu, D.-W. Zhang, Fabrication of 1D Te/2D ReS_2 mixed-dimensional van der Waals p-n heterojunction for high-performance phototransistor, ACS Nano 15 (2021) 3241–3250.
[27] Y. Yin, Y. Guo, D. Liu, C. Miao, F. Liu, X. Zhuang, Y. Tan, F. Chen, Z. Yang, Substrate-Free Chemical Vapor Deposition of Large-Scale III–V Nanowires for High-Performance Transistors and Broad-Spectrum Photodetectors, Advanced Optical Materials 10 (2022) 2102291.
[28] J. Lu, L. Zhang, C. Ma, W. Huang, Q. Ye, H. Yi, Z. Zheng, G. Yang, C. Liu, J. Yao, In situ integration of Te/Si 2D/3D heterojunction photodetectors toward UV-vis-IR ultra-broadband photoelectric technologies, Nanoscale 14 (2022) 6228–6238.
[29] W. Liu, Y. Yu, M. Peng, Z. Zheng, P. Jian, Y. Wang, Y. Zou, Y. Zhao, F. Wang, F. Wu, C. Chen, J. Dai, P. Wang, W. Hu, Integrating 2D layered materials with 3D bulk materials as van der Waals heterostructures for photodetections: current status and perspectives, InfoMat 5 (2023) e12470.
[30] B. Li, G. Shi, S. Lei, Y. He, W. Gao, Y. Gong, G. Ye, W. Zhou, K. Keyshar, J. Hao, P. Dong, L. Ge, J. Lou, J. Kono, R. Vajtai, P.M. Ajayan, 3D Band diagram and photoexcitation of 2D–3D semiconductor heterojunctions, Nano Lett. 15 (2015) 5919–5925.
[31] L.H. Zeng, D. Wu, S.H. Lin, C. Xie, H.Y. Yuan, W. Lu, S.P. Lau, Y. Chai, L.B. Luo, Z. J. Li, Y.H. Tsang, Controlled synthesis of 2D palladium diselenide for sensitive photodetector applications, Adv. Funct. Mater. 29 (2018) 1806878.
[32] T. Yu, F. Wang, Y. Xu, L. Ma, X. Pi, D. Yang, Graphene coupled with silicon quantum dots for high-performance bulk-silicon-based Schottky-Junction photodetectors, Adv. Mater. 28 (2016) 4912–4919.
[33] Z. Zheng, J. Yao, L. Zhu, W. Jiang, B. Wang, G. Yang, J. Li, Tin dioxide quantum dots coupled with graphene for high-performance bulk-silicon Schottky photodetector, Mater. Horiz. 5 (2018) 727–737.
[34] L. Zhao, Q. Shang, M. Li, Y. Liang, C. Li, Q. Zhang, Strong exciton-photon interaction and lasing of two-dimensional transition metal dichalcogenide semiconductors, Nano Res. 14 (2020) 1937–1954.
[35] B. Deng, V. Tran, Y. Xie, H. Jiang, C. Li, Q. Guo, X. Wang, H. Tian, S.J. Koester, H. Wang, J.J. Cha, Q. Xia, L. Yang, F. Xia, Efficient electrical control of thin-film black phosphorus bandgap, Nat. Commun. 8 (2017) 14474.
[36] R. Fei, L. Yang, Lattice vibrational modes and Raman scattering spectra of strained phosphorene, Appl. Phys. Lett. 105 (2014) 083120.
[37] Z. Lin, Z. Yang, J. Wang, S. Yang, De novo studies of working mechanisms for self-driven narrowband perovskite photodetectors, ACS Appl. Mater. Interfaces (2023) 14557–14565.
[38] H. Guo, W. Qi, New materials and designs for 2D-based infrared photodetectors, Nano Res. 16 (2022) 3074–3103.
[39] H.Y. Wang, Z.X. Li, D.Y. Li, P. Chen, L.J. Pi, X. Zhou, T.Y. Zhai, Van der Waals integration based on two-dimensional materials for high-performance infrared photodetectors, Adv. Funct. Mater. 31 (2021) 2103106.
[40] O. Lopez-Sanchez, D. Lembke, M. Kayci, A. Radenovic, A. Kis, Ultrasensitive photodetectors based on monolayer MoS_2, Nat. Nanotechnol. 8 (2013) 497–501.
[41] Z. Song, Y. Liu, Q. Wang, S. Yuan, Y. Yang, X. Sun, Y. Xin, M. Liu, Z. Xia, Self-powered photodetectors based on a ZnTe–TeO_2 composite/Si heterojunction with ultra-broadband and high responsivity, J. Mater. Sci. 53 (2018) 7562–7570.
[42] Y. Fang, Q. Dong, Y. Shao, Y. Yuan, J. Huang, Highly narrowband perovskite single-crystal photodetectors enabled by surface-charge recombination, Nat. Photonics 9 (2015) 679–686.
[43] A. Yazmaciyan, P. Meredith, A. Armin, Cavity enhanced organic photodiodes with charge collection narrowing, Adv. Opt. Mater. 7 (2019) 1801543.
[44] J. Wang, X. Xu, S. Xiao, Y. Li, W. Qian, J. Yu, K. Zhang, S. Yang, Self-driven perovskite dual-band photodetectors enabled by a charge separation reversion mechanism, Adv. Opt. Mater. 9 (2021) 2100517.
[45] M. Farronato, P. Mannocci, M. Melegari, S. Ricci, C.M. Compagnoni, D. Ielmini, Reservoir computing with charge-trap memory based on a MoS_2 channel for neuromorphic engineering, Adv. Mater. 35 (2022) 2205381.
[46] J.R. Yu, X.X. Yang, G.Y. Gao, Y. Xiong, Y.F. Wang, J. Han, Y.H. Chen, H. Zhang, Q. J. Sun, Z.L. Wang, Bioinspired mechano-photonic artificial synapse based on graphene/MoS heterostructure, Sci. Adv. 7 (2021) eabd9117.
[47] X. Liu, D. Wang, W. Chen, Y. Kang, S. Fang, Y. Luo, D. Luo, H. Yu, H. Zhang, K. Liang, L. Fu, B.S. Ooi, S. Liu, H. Sun, Optoelectronic synapses with chemical-electric behaviors in gallium nitride semiconductors for biorealistic neuromorphic functionality, Nat. Commun. 15 (2024) 7671.
[48] G. Kresse, J. Furthmüller, Efficiency of ab-initio total energy calculations for metals and semiconductors using a plane-wave basis set, Comput. Mater. Sci 6 (1996) 15–50.
[49] P.E. Blochl, Projector augmented-wave method, Phys. Rev. B Condens. Matter 50 (1994) 17953–17979.
[50] J.P. Perdew, K. Burke, M. Ernzerhof, Perdew, Burke, and Ernzerhof Reply, Phys. Rev. Lett. 80 (1998) 891.
[51] J.P. Perdew, K. Burke, M. Ernzerhof, Generalized gradient approximation made simple, Phys. Rev. Lett. 77 (1996) 3865–3868.
[52] R.M. Martin, G. Lucovsky, K. Helliwell, Intermolecular bonding and lattice dynamics of Se and Te, Phys. Rev. B 13 (1976) 1383–1395.
[53] Y. Wang, G. Qiu, R. Wang, S. Huang, Q. Wang, Y. Liu, Y. Du, W.A. Goddard, M. J. Kim, X. Xu, P.D. Ye, W. Wu, Field-effect transistors made from solution-grown two-dimensional tellurene, Nat. Electron. 1 (2018) 228–236.
[54] F. Wang, T. Zhang, R. Xie, Z. Wang, W. Hu, How to characterize figures of merit of two-dimensional photodetectors, Nat. Commun. 14 (2023) 2224.
[55] J. Yao, F. Chen, J. Li, J. Du, D. Wu, Y. Tian, C. Zhang, J. Yang, X. Li, P. Lin, A high-performance short-wave infrared phototransistor based on a 2D tellurium/MoS_2 van der Waals heterojunction, J. Mater. Chem. C 9 (2021) 13123–13131.
[56] N. Zhao, K. Wang, J. Li, 2D nonlayered tellurium nanosheets for self-powered photodetectors, Appl. Phys. A 129 (2023) 872.
[57] Z. Xie, C. Xing, W. Huang, T. Fan, Z. Li, J. Zhao, Y. Xiang, Z. Guo, J. Li, Z. Yang, B. Dong, J. Qu, D. Fan, H. Zhang, Ultrathin 2D Nonlayered tellurium nanosheets: facile liquid-phase exfoliation, characterization, and photoresponse with high performance and enhanced stability, Adv. Funct. Mater. 28 (2018) 1705833.
[58] Y. Du, B. Chang, J. Zhang, B. Li, X. Wang, First-principles study of the electronic structure and optical properties of GaN(0001) surface, Acta Phys. Sin. 61 (2012) 067101.
[59] J. Wang, M. Yuan, G. Tang, H. Li, J. Zhang, S. Guo, Two-dimensional electron gas in GaAs/$SrHfO_3$ heterostructure, J. Appl. Phys. 119 (2016) 235304.

[60] Z. Zhang, T. Wu, Z. Qin, M. Chen, W. Xiang, Z. Chen, Y. Wang, Z. Guo, T. Matsushima, L. Han, Synergistic improvement of structural ordering and interface binding of hole transport monolayer for efficient inverted perovskite solar cells, Adv. Energy Mater. 2500572 (2025).

[61] H.B. Michaelson, The work function of the elements and its periodicity, J. Appl. Phys. 48 (1977) 4729–4733.

[62] J.T. Trexler, S.J. Pearton, P.H. Holloway, M.G. Mier, K.R. Evans, R.F. Karlicek, Comparison of Ni/Au, Pd/Au, and Cr/Au metallizations for ohmic contacts to p-GaN, Mater. Res. Soc. Symp P. 449 (1997) 1091–1096, https://doi.org/10.1557/PROC-449-1091.

[63] J. Low, J. Yu, M. Jaroniec, S. Wageh, A.A. Al-Ghamdi, Heterojunction photocatalysts, Adv. Mater. 29 (2017) 1601694.